Broad spectrum attenuated total reflectance: numerical and experimental demonstration

E. Pisano

CONAHCYT-Centro de Investigación en Materiales Avanzados,
S.C. Subsede Monterrey, Alianza Norte 202, PIIT C.P. 66629, Apodaca, Nuevo León, Mexico.

F. Armenta-Monzón

Centro de Investigación en Materiales Avanzados,
S.C. Subsede Monterrey, Alianza Norte 202, PIIT, 66629, Apodaca, Nuevo León, México.

R. Israel Rodríguez-Beltrán

CONAHCYT - Centro de Investigación Científica y de Educación Superior de Ensenada, Unidad Monterrey,
Alianza Centro 504, PIIT, 66629, Apodaca, Nuevo León, México.

N. Ornelas-Soto

Tecnológico de Monterrey, Escuela de Ingeniería y Ciencias,
Av. Eugenio Garza Sada 2501, 64849, Monterrey, Nuevo León, México.

M. I. Mendivil Palma

Centro de Investigación en Materiales Avanzados, S.C. Subsede Monterrey,
Alianza Norte 202, PIIT 66629, Apodaca, Nuevo León, Mexico.

A. García-García

Centro de Investigación en Materiales Avanzados, S.C. Subsede Monterrey,
Alianza Norte 202, PIIT 66629, Apodaca, Nuevo León, Mexico.

R. Téllez-Limón

CONAHCYT - Centro de Investigación Científica y de Educación Superior de Ensenada,
Unidad Monterrey, Alianza Centro 504, PIIT, C.P. 66629, Apodaca, Nuevo León, México,
e-mail: rtellez@conahcyt.mx

Nano-optics is one of the most rapidly expanding fields in physics. Providing students with a basic knowledge of nano-optics and its practical applications, bridges the gap between theoretical concepts and real-world technological advancements, making the study of this branch of physics more tangible and exciting. In this study, we present a comprehensive analysis of the reflectivity of light from a thin-multilayered system across a broad spectrum. We theoretically examined the transmission and reflection of incident plane waves at interfaces between different media using the T-matrix method. We compared our theoretical findings with experimental results obtained from an attenuated total reflection (ATR) setup, which employed a supercontinuum laser as light source. This setup allowed us to observe both angular and spectral dependence of reflectivity. The sample under study, fabricated using e-beam physical vapor deposition, consisted of a BK-7 glass substrate, a 3 nm Cr layer, a 30 nm Au layer, and air as the superstrate. The obtained results demonstrate the accuracy of both, experimental and numerical methods. Our study not only serves as a valuable didactic resource, but also opens new perspectives for sensing applications where spectral shift of plasmonic resonances is a subject of interest.

1. Introduction

Physics is the cornerstone of all natural sciences, teaching us the fundamental laws that govern the universe. For students, an understanding of physics is not just an academic requirement; it's a critical tool that paves the way for innovation and technological advancements. By grasping the principles of physics, students gain the ability to solve complex problems and contribute to the evolution of various technologies.

In recent years, the study and development of thin-multilayered systems have found applications across diverse fields, highlighting their versatility and importance. For instance, multilayer configurations are widely used in optical coatings for lenses [1] and spectacle glasses [2], as well as optical filters [3]. They also play a crucial role in energy-efficient windows, where films are utilized to minimize heat loss [4,5], the composition of transistors and integrated circuits [6,7], the configuration of fiber lasers [8,9], the instru-

mentation for X-ray astronomy [10,11], and the development of micro-LEDs for display applications [12], among others.

Notably, nanotechnology has been crucial in advancing our comprehension and implementation of multilayered structures. As a result, scientific research done in this regard includes: characterizing optical coatings [13,14], testing novel sensitive materials [15,16], developing advanced optical sensors [17,18], proposing integrated optical devices for on-chip applications [19,20], designing photonic crystals for optical filter applications [21], predicting the behavior of light modes in a waveguide [22], designing single-mode plasmonic bandpass filters [23] and optimizing optical cavities [24], to name a few.

Manipulation of electromagnetic fields at the nanoscale has played a fundamental role developing highly sensitive devices consisting of multilayer systems. Such is the case of the propagation and control of surface plasmon polaritons (SPPs), which are surface electromagnetic waves confined to the interface formed by two media (layers), one being a conductor and the other a dielectric [25]. As the excitation of SPPs requires fulfilling the wave vector matching condition between the incident light and the SPPs, the chosen excitation method will depend on the purpose of application.

SPPs can be excited through diverse methods. Among them, the excitation of SPPs with light through the attenuated total reflection (ATR) configuration stands out for its simplicity. In this method, a polarized light beam is incident onto a thin metallic film deposited on a glass prism. The coupling of the light beam to SPPs can be achieved by varying the angle of incidence, i.e., through the ATR mechanism. The coupling of light to SPPs occurs at an angle called the angle of resonance, where the wave vectors of the incident light match those of the SPPs [26].

The ATR configuration has expanded its capabilities beyond its original design, being nowadays the base setup for novelty sensors based on the Surface Plasmon Resonance (SPR) phenomenon. A notable advancement has been the addition of the spectral analysis for the SPR-based sensors. This approach adds a broad-spectrum light source and a spectrometer to the original design. Instead of relying solely on the resonance angle, this analysis measures the drop in intensity for specific wavelengths within the analyzed spectrum [27-30]. These minimums in intensity are highly sensitive to changes in the properties of the media that make up the interface where plasmonic coupling occurs, which represents an attractive feature for SPR-based sensors.

Some studies of SPR-based sensors employing the ATR configuration performing spectral analysis have been reported in the literature. For instance, in Ref. [31], Chlebus and coauthors determined the dielectric function of thin metal films by measuring the wavelength dependence of the reflectance ratio of p- and s-polarized components from a white light source subjected to the SPR phenomenon at different angles of incidence. In Ref. [32] they used the same SPR configuration with a white light source to determine the spectral phase shift due to the presence of an analyte (NaCl solutions)

at different concentrations. In Ref. [33], Arora et al. demonstrated numerically and experimentally the enhancement of the SPR sensing using a broadband light source in the ATR configuration, with the addition of a plasmonic nanograting on top of a gold (Au) thin layer. In Ref. [34], Shalabney and Abdulhalim improved the sensitivity of an SPR-based sensor focusing on spectral interrogation mode. This study showed that adding a thin dielectric layer with a high refractive index on top of the metallic layer in the SPR-based sensor caused a red shift on the resonance wavelength, then obtaining a sharper resonance dip and enhancement to the spectral sensitivity. Also, in Ref. [35], Pavelkin presents a theoretical study to obtain the ATR spectra of plasmonic structures from visible to infrared spectral regions.

To understand the behavior of the SPR phenomenon from the spectrum analysis approach, efficient and reliable numerical methods are essential. In this regard, the T-matrix method has been employed. This method is a powerful mathematical formalism widely used in electromagnetism to describe the transmission and reflection of incident plane waves at the interface between two different media. While it can be applied to single-layer configurations, its true strength lies in its ability to analyze multilayered structures without the necessity of high computational resources. At each interface between adjacent layers, electromagnetic waves undergo changes in phase and amplitude dictated by the optical properties of the layers, such as their refractive index and thickness [36]. In the end, the properties of each layer and the amplitudes of the incident and transmitted waves can be related by a sole 2×2 matrix by multiplying the matrices for each layer [19].

In this work, we present a concise and comprehensive overview of the mathematical formulation of the T-matrix method, including the interpretation of the dispersion curves and reflectivity maps. Moreover, we have specifically implemented the T-matrix method for the spectral and angular analysis of the ATR configuration for a glass-chromium-gold-air system. We provide a discussion of the experimental setup and compare results achieved with the implemented analytical method with those experimentally obtained.

2. Numerical method: T-matrix method

Let us consider the system of N thin layers depicted in Fig. 1. The system is invariant along the out-of-plane y direction. Each layer has a thickness t_m and dielectric constant $\varepsilon_m(\omega)$, for $m = [1, 2, ..., N]$. Both, substrate (medium 1) and superstrate (medium N) are semi-infinite. The interface between two adjacent layers along the z direction, is denoted by d_m, with $m = [1, 2, ..., N-1]$.

To compute the modes supported by the system, as well as the reflection and transmission of light, we can propose a general solution for the electromagnetic waves propagating at each layer, as the superposition of propagative and counter-propagative harmonic plane waves. Considering that the thickness of the layers is shorter than the wavelength of

light, $t_m < \lambda$, (paraxial approximation) this superposition can be expressed as

$$
\psi_m(x, z, \omega) = A_m e^{i(\beta_m x + \alpha_m z)} e^{i\omega t}
$$
$$
+ B_m e^{i(\beta_m x - \alpha_m z)} e^{i\omega t}, \quad (1)
$$

where A_m and B_m are the amplitudes of propagative and counter-propagative plane waves, respectively; ω is the frequency of the harmonic plane-wave, and α_m and β_m are the components of the wavevector, $\mathbf{k}_m$, along z and x directions, respectively. Considering the normal to the system along the z axis, the wavevectors are given by

$$
\alpha_m = k_0 n_m \cos\theta = \frac{2\pi}{\lambda} n_m \cos\theta, \quad (2)
$$

$$
\beta_m = k_0 n_m \sin\theta = \frac{2\pi}{\lambda} n_m \sin\theta, \quad (3)
$$

being θ the angle between the z axis and wavevector $\mathbf{k}_m$, and $n_m = \sqrt{\varepsilon_m(\omega)\mu_m(\omega)}$ the refractive index of the m−th layer. At optical frequencies, the magnetic permeability $\mu_m(\omega) \approx 1.0$, hence we consider only the electric permittivity for the refractive index, $n_m = \sqrt{\varepsilon_m(\omega)}$.

From Maxwell equations, the components of the wavevector satisfy the constitutive relationship

$$
\beta_m(\alpha_m) = \sqrt{k_0^2 \varepsilon_m(\omega) - \alpha_m^2}, \quad (4)
$$

and from continuity of tangential components of the electromagnetic field, at the interface between two adjacent layers (d_m) must be satisfied the boundary conditions [37]

$$
\psi_m(x, z, \omega)|_{z=d_m} = \psi_{m+1}(x, z, \omega)|_{z=d_m}, \quad (5)
$$

$$
\frac{1}{\nu_m} \frac{\partial \psi_m(x, z, \omega)}{\partial z}\bigg|_{z=d_m} = \frac{1}{\nu_{m+1}} \frac{\partial \psi_{m+1}(x, z, \omega)}{\partial z}\bigg|_{z=d_m}, \quad (6)
$$

with $\nu_m = 1$ for s polarization and $\nu_m = \varepsilon_m(\omega)$ for p polarization.

Considering that the propagation constant at each interface must be the same along the x direction ($\beta_m = \beta_{m+1}$), substitution of Eq. (1) into boundary conditions given by Eqs. (5) and (6), leads to a two-equation system relating amplitudes and propagation constants of waves in layers m and $m + 1$, given by

$$
A_m e^{ik_m} + B_m e^{-ik_m}
$$
$$
= A_{m+1} e^{ik_{m+1}} + B_{m+1} e^{-ik_{m+1}}, \quad (7)
$$

$$
A_m \gamma_m e^{ik_m} - B_m \gamma_m e^{-ik_m}
$$
$$
= A_{m+1} e^{ik_{m+1}} - B_{m+1} e^{-ik_{m+1}}, \quad (8)
$$

with $k_m = \alpha_m d_m$, $k_{m+1} = \alpha_{m+1} d_m$, and $\gamma = (\nu_{m+1}/\nu_m)(\alpha_m/\alpha_{m+1})$. Equations (7) and (8) can be written in a matrix form as

$$
\begin{pmatrix} A_{m+1} \\ B_{m+1} \end{pmatrix} = \frac{1}{2} (\mathbf{T}_m) \begin{pmatrix} A_m \\ B_m \end{pmatrix}, \quad (9)
$$

where

$\mathbf{T}_m$

$$
= \begin{pmatrix} (1+\gamma_m)e^{i(k_m-k_{m+1})} & (1-\gamma_m)e^{-i(k_m+k_{m+1})} \\ (1-\gamma_m)e^{i(k_m+k_{m+1})} & (1+\gamma_m)e^{-i(k_m-k_{m+1})} \end{pmatrix}. \quad (10)
$$

As the system has N layers, we can extend the previous result to $N - 1$ interfaces by multiplying the $\mathbf{T}_m$ matrix of each interface, being obtained a general expression relating the amplitudes of plane waves of the substrate and superstrate:

$$
\begin{pmatrix} A_N \\ B_N \end{pmatrix} = \prod_{m=1}^{N-1} (\mathbf{T}_m) \begin{pmatrix} A_1 \\ B_1 \end{pmatrix}
$$
$$
= \begin{pmatrix} t_{1,1} & t_{1,2} \\ t_{2,1} & t_{2,2} \end{pmatrix} \begin{pmatrix} A_1 \\ B_1 \end{pmatrix}. \quad (11)
$$

Relationship given in Eq. (11) is known as the T-matrix method, a recursive algorithm that reduces the multilayered system, into a two-medium problem.

2.1. Dispersion curves

From linear algebra, it is well known that a proper vector is a set of values that remains unchanged after a linear transformation. For our multilayered structure, these proper vectors correspond to the modes supported by the system. In other words, waves whose amplitude and polarization remain unchanged when light propagates through the system.

To find the proper modes of the system, we must impose the boundary conditions $A_1 = B_N = 0$, *i.e.*, no external light sources are considered. This assumption means that, regardless of incident light, solutions to the matrix Eq. (11) lead to the modes supported by the multilayered structure. Hence

$$
\begin{pmatrix} A_N \\ 0 \end{pmatrix} = \begin{pmatrix} t_{1,1} & t_{1,2} \\ t_{2,1} & t_{2,2} \end{pmatrix} \begin{pmatrix} 0 \\ B_1 \end{pmatrix}, \quad (12)
$$

and from this equation is obtained

$$
0 = t_{2,2} \frac{A_N}{t_{1,2}}. \quad (13)
$$

As amplitudes A_N and B_1 should be different from zero, after computing the general $\mathbf{T}$ matrix, Eq. (13) is satisfied when $t_{2,2}$ vanishes and $t_{1,2}$ is different from zero. Hence, the proper modes of the system can be obtained through

$$
t_{2,2} = 0. \quad (14)
$$

In other words, all the values of $\beta(\alpha)$ given by relationship (4), satisfying Eq. (14) correspond to the modes or resonances of the multilayered structure.

Equation (14) cannot be always analytically solved and numerical methods are required. For instance, when any of the layers presents in a complex dielectric constant, such as metallic layers, it is obtained a complex transcendental function. For this case, a simple and fast way to visualize an approximation of the proper modes is by evaluating different values of β in a wavelength spectral range and plot the absolute value of the term $t_{2,2}$.
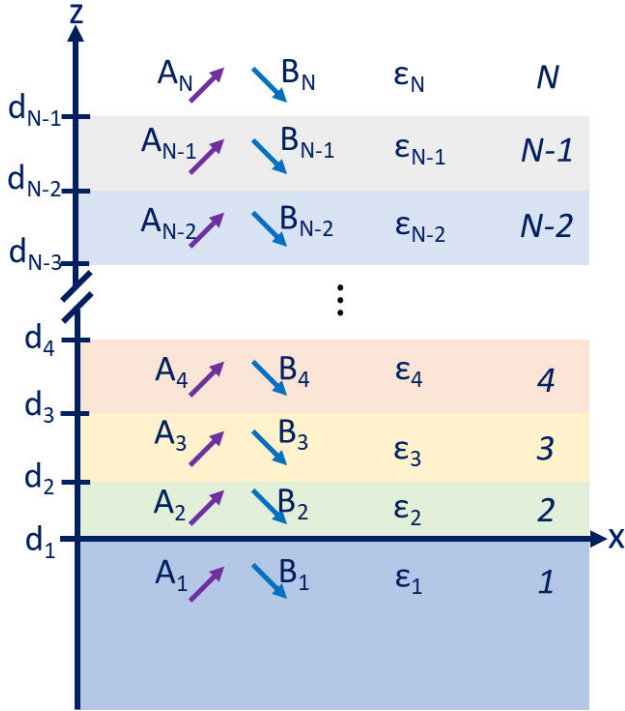
FIGURE 1. Schematic representation of a system of N layers invariant along the out-of-plane y direction. Both, substrate and superstrate are semi-infinite media. There are $N-1$ interfaces along z axis located at positions d_m, for $m = 1, 2, ..., N - 1$.

2.2. Reflection and transmission

To compute the portion of light reflected or transmitted by a multilayered structure, we can also use the T-matrix equation. For instance, let us assume that the system is illuminated from the substrate with an incident plane wave forming an angle θ_{inc} measured from the normal to the surface (parallel to z direction). For this situation, it is clear that $B_N = 0$, as no light impinges from the superstrate. To obtain a normalized value of the reflection and transmission, let us assume a unitary amplitude for the incident plane wave, $A_1 = 1$. From Fig. 1 we can define the reflection and transmission coefficients as $r = B_1$ and $t = A_N$. Then, from Eq. (11) we have

$$\begin{pmatrix} t \\ 0 \end{pmatrix} = \begin{pmatrix} t_{1,1} & t_{1,2} \\ t_{2,1} & t_{2,2} \end{pmatrix} \begin{pmatrix} 1 \\ r \end{pmatrix}. \tag{15}$$

Thus, reflection and transmission values are given by

$$R = |r|^2 = \left| -\frac{t_{2,1}}{t_{2,2}} \right|^2, \tag{16}$$

and

$$T = |t|^2 = \left| \frac{t_{1,1}t_{2,2} - t_{1,2}t_{2,1}}{t_{2,2}} \right|^2. \tag{17}$$

We must remark that the polarization dependence on the reflection and transmission is already contained in the elements of the matrix. From Eq. (3), the propagation constant

of reflected light can be expressed as a function of the incidence angle, θ_{inc}, by

$$\beta_{sub} = \frac{2\pi}{\lambda} n_{sub} \sin \theta_{inc}. \tag{18}$$

From Eq. (18), two limit values of θ_{inc} arise:

- $\theta_{inc} = \pi/2$. For an incidence angle parallel to the x direction (grazing angle), the propagation constant, $\beta_{sub} = (2\pi/\lambda) n_{sub}$, corresponds to the propagation constant of light in the substrate. This value is known as "substrate light-line".

- $\theta_{inc} = \theta_c = \arcsin(n_{sub}/n_{sub})$. When the incidence angle is equal to the critical angle (defined from Snell law), the propagation constant, $\beta_{sub} = (2\pi/\lambda) n_{sup}$, corresponds to light propagating through the superstrate. This value is known as "superstrate light-line".

Hence, if we illuminate the system at an angle satisfying the condition for total internal reflection ($\theta_{inc} > \theta_c$), the propagation constant of the reflected wave varies from β_{sup} to β_{sub}. This situation means that the effective index of reflected waves lays between the light-lines of substrate and superstrate media, $n_{sub} > n_{eff} > n_{sup}$.

3. Experimental methods

3.1. Fabrication of the sample

The sample under study is a four-layered structure consisting of a BK-7 glass substrate ($n_{sub} = 1.515$), a thin layer of Cr of thickness 3 nm, on top of which is placed an Au layer of 30 nm in thickness, and the superstrate is air ($n_{sup} = 1.0$), as schematically depicted in Fig. 2a).

For the fabrication of this multilayered sample, e-beam physical vapor deposition technique was used (EBPVD; Torr-international®, EB4P7CC-3kW-LL®). Before deposition, the substrate was cleaned with an ultrasonic bath using isopropyl alcohol and deionized water. To ensure the adherence of the Au layer over the substrate, we deposited a thin film of 3 nm of Cr (99.95% pure, KurtLeskser®) with a pressure of 5.57×10^{-7} Torr, a current of 16 mA and a rate of deposition of 0.1 Å/s. Afterwards, the Au film of 30 nm of thickness (99.9% pure, American Elements®) was deposited at a pressure of 3×10^{-6} Torr, 100 mA, and 0.6 Å/s deposition rate.

3.2. Broad spectrum ATR

The experimental setup, as depicted in Fig. 2b), consists of an ATR setup [38,39], with the modification of the illumination source and spectrometer instead of a power meter. The fabricated sample was attached to a BK-7 glass prism ($n_{prism} = 1.515$) with immersion oil of refractive index $n_{oil} = 1.512$. The prism with the sample was mounted on a two-rotation coaxial goniometric stage system. The first stage was employed to rotate the prism, *i.e.*, to control the
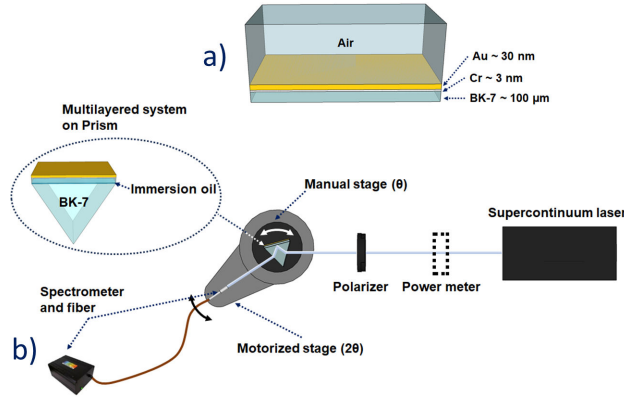
FIGURE 2. a) Schematic representation of a four-layered system. The system consisted of a 30 nm Au layer and a 3 nm Cr layer on top of a BK7 glass substrate ($n_{sub} = 1.515$), with air as superstrate ($n_{sup} = 1.0$). b) Schematic of the broad spectrum ATR setup. The sample was attached with immersion oil ($n_{oil} = 1.512$) on top of a BK7 prism ($n_{prism} = 1.515$). A p-polarized collimated beam from a supercontinuum laser was employed as light source. The manual stage controls the incidence angle, while the motorized stage was adjusted for each incidence angle to measure the output signal (reflectivity) with a fibered spectrometer.

incidence angle (θ_{inc}), while the second high-resolution motorized stage (Thorlabs®) was used to align the detector, performing a movement of $2\theta_{inc}$. The detector consisted of a multimode optical fiber plugged with a SMA connector to an optical spectrometer (StellarNet® BlackComet) with a spectral detection range from 360 nm to 1100 nm. To illuminate the sample on the prism, we used a broad-spectrum collimated beam from a supercontinuum laser (Leukos® Electro-VIS-IR 430), with an emission spectral range from 450 nm to 2400 nm. The beam was p-polarized with the assistance

of a broad-band linear polarizer. We limited our measurements to a spectral range from 480 nm to 900 nm, where the laser emission was flatter. Additionally, a power meter (PM1000USB, Thorlabs®) was used to measure the average power of light beam at the output of the laser. The reflectivity of the sample was normalized to the reflectivity of the prism without the sample. Experiments were performed at room temperature and ambient humidity.

4. Results

By means of the T-matrix method, we numerically characterized the four-layered structure described in Sec. 3.1 [Fig. 2a)]. We computed the dispersion curves of the system and its reflectance when illuminating from the substrate. For these calculations, the values for the dielectric function of Cr were taken from Ref. [40], while the values for Au were obtained by following the model described in Refs. [41-43]. Then, to demonstrate the accuracy of the theoretical results, we experimentally characterized the angular reflection of the multilayer structure using an ATR setup with a supercontinuum laser [Fig. 2b)], and compare the results.

4.1. Dispersion curves

The results shown in Fig. 3a) correspond to $|t_{22}|$, the complex magnitude of Eq. (14), computed in the spectral wavelength range from 480 nm to 900 nm, and propagation constant in the range $\mathbb{R}\{\beta\} = [0, 3] \times 10^7$ m^{-1}. Logarithmic scale was used to improve the contrast of the map. Minima values correspond to the modes of the four-layered system. Black dotted and dashed curves correspond to superstrate (air) and substrate (glass) light-lines, β_{sup}, β_{sub}, respectively.
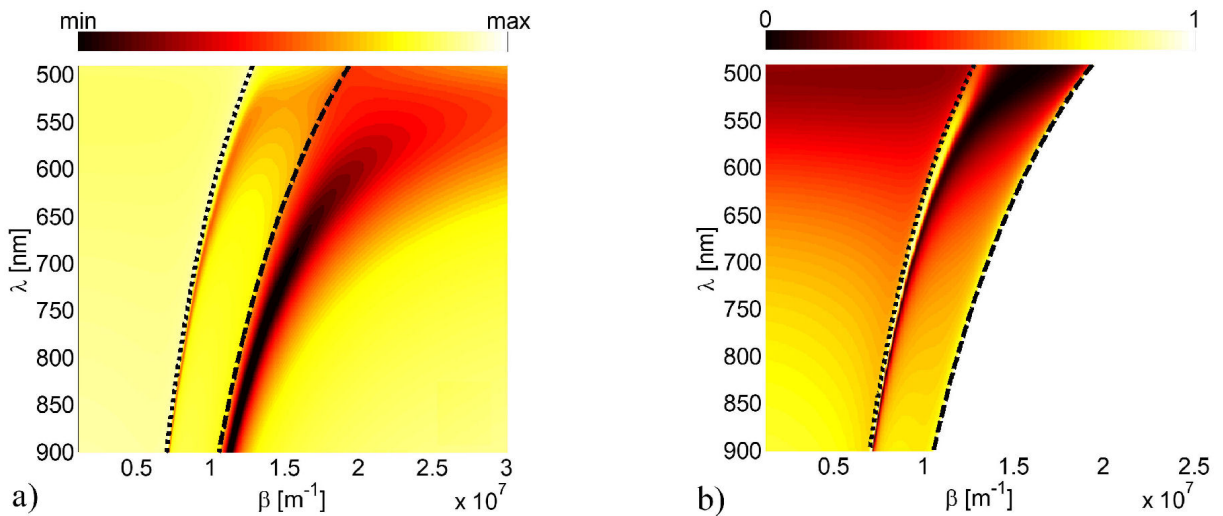

FIGURE 3. a) Dispersion curves of the BK-7 glass/Cr/Au/air system computed with the T-matrix method. Black-dotted and black-dashed curves correspond to air and glass light-lines, respectively. The two main minimum branches correspond to the modes of the system. b) Reflectivity as a function of the propagation constant. Black-dotted and black-dashed curves correspond to air and glass light-lines, respectively. A broad minima reflection is observed between air and glass light-lines, corresponding to the attenuated total reflectance.
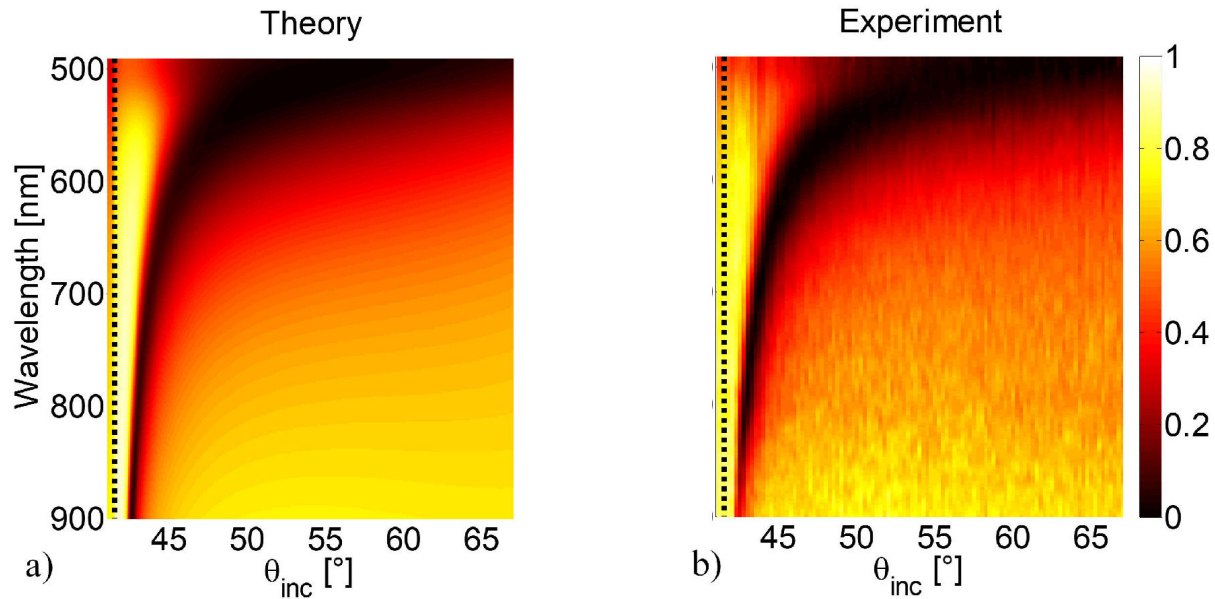
FIGURE 4. Reflectivity spectra as a function of incidence angle. a) Theoretical results obtained with the T-matrix method, and b) experimental results obtained with the broad spectrum ATR setup. The black-dashed line corresponds to critical angle (substrate light-line).

Two main broad branches of minimum values are observed in Fig. 3a), one between air and glass light-lines, and a second one beyond the glass light-line. Modes, whose wavevector is between β_{sub} and β_{sub} ($\beta_{\text{sub}} < \beta < \beta_{\text{sub}}$), correspond to waves that are radiated into the glass substrate. Modes whose wavevector is larger than β_{sub} are modes confined into Cr and Au thin layers. In other words, two modes are supported by the system: one mode whose energy is radiated to the glass substrate, and a second mode confined in the metallic layers.

4.2. Reflectance of the system

Using relationship (16), the reflectivity of the system can be determined as a function of the propagation constant and wavelength. The resulting plot is shown in Fig. 3b). In this map, it is observed that for propagation constants beyond the glass light-line (dashed curve), the reflectivity values do not provide information about confined modes, because these modes cannot be excited by illuminating from the substrate nor the superstrate. For light radiated into the substrate ($\beta_{\text{sub}} < \beta < \beta_{\text{sub}}$), a broad minimum band in the reflectivity is observed. This band of minimum values becomes narrower as the wavelength increases. For light radiated into the air superstrate ($\beta < \beta_{sup}$), reflectivity vanishes for wavelengths $\lambda < 530$ nm, close to the spectral region where intraband transitions for Au take place.

A more intuitive way to understand the map in Fig. 3b) is by plotting the reflectivity as a function of the incidence angle of light, θ_{inc}. To this purpose, we used the relationship given in Eq. (3) to define the values of Eq. (16).

The resulting map, shown in Fig. 4a), corresponds to the reflectivity for a spectral range varying from 480 nm to 900 nm for incidence angles between 37° and 67°. The vertical

dashed line corresponds to the critical angle (air light-line) for a BK-7 glass/air interface ($\theta_c = 41.47$). Minima values correspond to ATR expected for a metal/dielectric (Au/BK-7) interface due to the excitation of SPPs [26,38,39,44]. As observed, for the BK-7/Cr/Au/air system, when the wavelength increases, the band of minimum values becomes narrower and approaches to the critical angle. When the wavelength is shorter, the band of minimum values becomes wider and can be reached at almost every angle, *i.e.*, for shorter wavelengths, the radiated mode can be excited with light impinging from the substrate at almost any angle above the critical angle. This situation means that, for sensing applications, it is better to operate at longer wavelengths, where the SPR excitation is achieved at a shorter domain of incidence angles.

To corroborate the numerical results, we measured the reflectivity of the multilayered system with the broad spectrum ATR setup described in Sec. 3.2. The results are shown in Fig. 4b). A direct observation shows a good agreement between theoretical and experimental angular reflectivity spectra.

To compare the theoretical and experimental results, we plotted the reflectance at a fixed wavelength ($\lambda = 633$ nm) as a function of incidence angle, θ [Fig. 5a)]. Red solid curves correspond to theoretical values and blue dotted curves to experimental data. The vertical dashed line corresponds to the critical angle. Theoretical results exhibit a minimum reflectance at $\theta = 44.8°$, while experimental results show a minimum at $\theta = 44.75°$. The difference between these values arise from angular resolution of the experimental setup. Also, small amplitude discrepancies are due to signal scattering caused by the roughness of the sample.

In Fig. 5b) are compared theoretical (red curve) and experimental (blue dotted curve) reflectances as a function of wavelength at a fixed incidence angle $\theta = 45°$. Theoretical
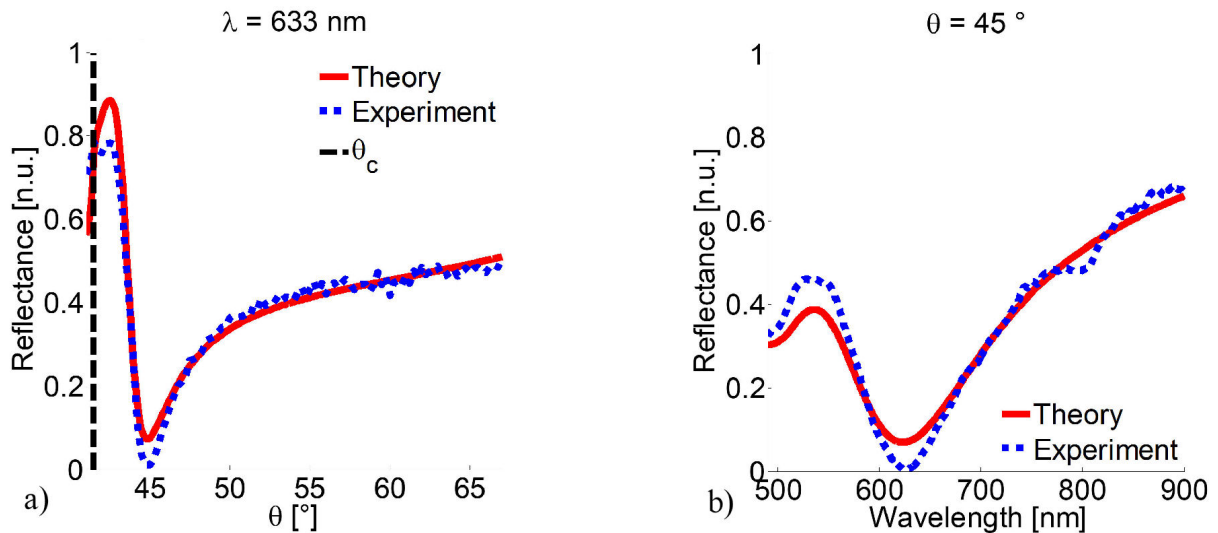
FIGURE 5. Comparison of theoretical (red curve) and experimental (blue dotted curve) reflectivity curves extracted from maps of Fig. 4. a) Reflectivity as a function of incidence angle for a fixed wavelength at $\lambda = 633$ nm. Vertical dashed line correspond to the critical angle θ_c. b) Reflectivity as a function of incidence wavelength for a constant incidence angle at $\theta_{\text{inc}} = 45°$.

results present a minimum reflectance around $\lambda = 623$ nm and experimental data at $\lambda = 625$ nm. As light scattering depends on the wavelength, there are larger discrepancies in amplitude.

5. Conclusions

The comprehensive analysis presented in this work offers valuable insights into the behavior of light when interacting with a thin-multilayered system. As demonstrated, T-matrix method is an efficient and reliable numerical approach that provides information about the physical behaviour of multilayered structures, requiring minimal computational resources. With this numerical method, we were able to theoretically predict the dispersion curves and reflection spectra of the system as a function of incidence angle. These theoretical predictions were subsequently validated through experimental measurements using the broad spectrum ATR setup.

For the multilayered structure (BK7-Cr-Au-Air) under study, the derived dispersion curves provided a clear understanding of the modes supported in this system, including a radiative mode and a confined mode. The reflectivity maps numerically generated, highlight the conditions for mode coupling from the substrate (radiated mode), as a function of wavelength and incident angle, simultaneously.

Angular and spectral dependence for mode coupling was experimentally demonstrated through the ATR setup illuminated with the supercontinuum laser. Theoretical predictions were in good agreement with the experimental results.

The performance of the ATR system was improved by employing the collimated beam from the supercontinuum laser and spectrometer for signal detection. The reflectivity maps obtained with this setup, offer a simultaneous view of angular and spectral dependence of reflectance minima.

This research not only emphasizes the potential of the ATR setup as a significant advancement for sensing applications. It also serves as a valuable didactic resource for academic and scientific community requiring a theoretical and experimental understanding about light interaction in multilayered systems, subject of interest in the realms of plasmonics and metaphotonics.

Acknowledgments

1. M.-X. Li *et al.*, Research on wavelength division film of glasses based on 3D technology in cinema, In J. Chu and H. Jiang, eds., Sixth Symposium on Novel Optoelectronic Detection Technology and Applications, **vol. 11455**, International Society for Optics and Photonics (SPIE, 2020) p. 114550G, `https://doi.org/10.1117/12.2558372`.

2. S. M. Lafta, A. M. Naji, and N. J. Mohammed, Antireflective and Hard Multicoat Design for Allyl Diglycol Carbonate Plastic Spectacle Lenses, *Key Eng. Mater.* **937** (2022) 139, `https://doi.org/10.4028/p-250jz8`

3. T. Palavets and M. Rosenfield, Blue-blocking Filters and Digital Eyestrain, *Optom. Vis. Sci.* **96** (2019) 48, `https://doi.`

org/10.1097/OPX.0000000000001318

4. M. A. Zahid *et al.*, Anti-reflective coating and cooling technique for innovative photovoltaic system in tropical region, *J. Power Sourc.* **564** (2023) 232812, https://doi.org/10.1016/j.jpowsour.2023.232812

5. X. Hong *et al.*, Design, fabrication and energy-saving evaluation of five-layer structure based transparent heat mirror coatings for windows application, *Build. Simul.* **16** (2023) 2333, https://doi.org/10.1007/s12273-022-0973-1.

6. J. Y. Lee and S. Y. Lee, Mechanism of Extraordinary High Mobility in Multilayered Amorphous Oxide Thin Film Transistor, *IEEE Trans. Electron Dev.* **68** (2021) 5618, https://doi.org/10.1109/TED.2021.3115732

7. S. Chen, *et al.*, Ultrahigh Strain-Insensitive Integrated Hybrid Electronics Using Highly Stretchable Bilayer Liquid Metal Based Conductor, *Adv. Mater.* **35** (2023) 2208569, https://doi.org/10.1002/adma.202208569

8. L. Rodríguez-Morales *et al.*, Experimental and theoretical study of a novel input polarization-independent nonlinear optical loop mirror with elliptical birefringence, *Opt. Laser Technol.* **163** (2023) 109454, https://doi.org/10.1016/j.optlastec.2023.109454

9. M. M. Fadhali, Theoretical optimization of cavity configurations for fiber lasers: enhancement of mode oscillation and slow-light effect, *Laser Phys.* **33** (2023) 055101, https://doi.org/10.1088/1555-6611/acc021

10. S. S. Panini *et al.*, Development of multilayer mirrors for space-based astronomical X-ray optics, *J. Opt.* **47** (2018) 91, https://doi.org/10.1007/s12596-017-0444-8

11. B. Mondal *et al.*, DarpanX: A python package for modeling X-ray reflectivity of multilayer mirrors, *Astron. Comput.* **34** (2021) 100446, https://doi.org/10.1016/j.ascom.2020.100446

12. W.-C. Miao *et al.*, Modified Distributed Bragg Reflectors for Color Stability in InGaN Red Micro-LEDs, *Nanomater.* **13** (2023), https://doi.org/10.3390/nano13040661

13. W. M. E. M. M. Daniyal *et al.*, Design and Optimization of Surface Plasmon Resonance Spectroscopy for Optical Constant Characterization and Potential Sensing Application: Theoretical and Experimental Approaches, *Photonics* **8** (2021) 361, https://doi.org/10.3390/photonics8090361

14. I. S. Khasanov *et al.*, Optical Characterization of Thin Films by Surface Plasmon Resonance Spectroscopy Using an Acousto-Optic Tunable Filter, *Materials* **16** (2023) 1820, https://doi.org/10.3390/ma16051820

15. W. M. E. M. M. Daniyal *et al.*, Surface plasmon resonance assisted optical characterization of nickel ion solution and nanocrystalline cellulose-graphene oxide thin film for sensitivity enhancement analysis, *Phys. Rev. B Condens.* **646** (2022) 414292, https://doi.org/10.1016/j.physb.2022.414292

16. F. B. K. Eddin *et al.*, Plasmonic Refractive Index Sensor Enhanced with Chitosan/Au Bilayer Thin Film for Dopamine Detection, *Biosensors* **12** (2022), https://doi.org/10.3390/bios12121124

17. G. Morales-Luna *et al.*, Plasmonic biosensor based on an effective medium theory as a simple tool to predict and analyze refractive index changes, *Opt. Laser Technol.* **131** (2020) 106332, https://doi.org/10.1016/j.optlastec.2020.106332

18. M. Herrera-Domínguez *et al.*, Development of a surface plasmon resonance based immunosensor for diclofenac quantification in water, Chemosphere **336** (2023) 139156, https://doi.org/10.1016/j.chemosphere.2023.139156

19. R. Téllez-Limón and R. Salas-Montiel, Nanowires Integrated to Optical Waveguides, In X. Peng, ed., Nanowires, chap. 8 (IntechOpen, Rijeka, 2021), https://doi.org/10.5772/intechopen.95689.

20. M.-U. A. Abdulkareem *et al.*, Integrated Optical Filters with Hyperbolic Metamaterials, *Nanomater.* **13** (2023) 759, https://doi.org/10.3390/nano13040759

21. F. S. Saeidi and M. Moradi, Designing a Multi-Periodic Photonic Crystal with Adjustable Transmission Peak for Optical Filter Applications, *J. Nanostruct.* **13** (2023) 66, https://doi.org/10.22052/JNS.2023.01.008

22. I. Haddouche and L. Cherbi, Comparison of finite element and transfer matrix methods for numerical investigation of surface plasmon waveguides, *Opt.Commun.* **382** (2017) 132, https://doi.org/10.1016/j.optcom.2016.07.068.

23. S. Khani, M. Danaie, and P. Rezaei, Design of a Single-Mode Plasmonic Bandpass Filter Using a Hexagonal Resonator Coupled to Graded-Stub Waveguides, *Plasmonics* **14** (2019) 53, https://doi.org/10.1007/s11468-018-0777-4

24. A. Bezza, A. Cherifi, and B. Bouhafs, Designing high sensitivity surface plasmon resonance sensor using a left-handed material layer, *Rev. Mex. Fis.* **69** (2023) 021002 1, https://doi.org/10.31349/RevMexFis.69.021002

25. V. M. Agranovich and A. A. Maradudin, Surface Polaritons (Elsevier Science, North Holland, 2012).

26. S. A. Maier, Plasmonics: Fundamentals and Applications (Springer, New York, 2010), https://doi.org/10.1007/0-387-37825-1.

27. A. Kocabas, S. S. Senlik, and A. Aydinli, Slowing Down Surface Plasmons on a Moiré Surface, *Phys. Rev. Lett.* **102** (2009) 063901, https://doi.org/10.1103/PhysRevLett.102.063901

28. S. Balci *et al.*, Direct imaging of localized surface plasmon polaritons, *Opt. Lett.* **36** (2011) 3401, https://doi.org/10.1364/OL.36.003401

29. R. Chuliá-Jordán and A. Unger, Comparison of the Different Bandgap Cavities in a Metallic Four-Mode Plasmonic Structure, *Plasmonics* **10** (2015) 429, https://doi.org/10.1007/s11468-014-9824-y

30. F. M. Balci *et al.*, Laser assisted synthesis of anisotropic metal nanocrystals and strong light-matter coupling in decahedral bimetallic nanocrystals, *Nanoscale Adv.* **3** (2021) 1674, https://doi.org/10.1039/D0NA00829J

31. R. Chlebus *et al.*, Surface Plasmon Resonance Based Measurement of the Dielectric Function of a Thin Metal Film, *Sensors* **18** (2018) 3693, https://doi.org/10.3390/s18113693

32. P. Hlubina and D. Ciprian, Spectral Phase Shift of Surface Plasmon Resonance in the Kretschmann Configuration: Theory and Experiment, *Plasmonics* **12** (2017) 1071, `https://doi.org/10.1007/s11468-016-0360-9`

33. P. Arora *et al.*, Dispersion engineering with plasmonic nano structures for enhanced surface plasmon resonance sensing, *Sci. Rep.* **8** (2018) 9060, `https://doi.org/10.1038/s41598-018-27023-x`

34. A. Shalabney and I. Abdulhalim, Figure-of-merit enhancement of surface plasmon resonance sensors in the spectral interrogation, *Opt. Lett.* **37** (2012) 1175, `https://doi.org/10.1364/OL.37.001175`

35. R. A. Pavelkin, Excitation of the broadband surface plasmon polaritons in planar metal-dielectric structures, In V. L. Derbov, ed., Laser Physics, Photonic Technologies, and Molecular Modeling, **vol. 12193**, International Society for Optics and Photonics (SPIE, 2022) p. 121930A, `https://doi.org/10.1117/12.2623149.`

36. S. A. Furman and A. V. Tikhonravov, Basics of optics of multilayer systems (Editions Frontieres, Paris, 1992).

37. J. D. Jackson, Classical Electrodynmics (John Wiley & Sons, Inc., New York, 1962).

38. E. Kretschmann and H. Raether, Notizen: Radiative Decay of Non Radiative Surface Plasmons Excited by Light, *Z. für Naturforsch. A* **23** (1968) 2135, `https://doi.org/10.1515/zna-1968-1247`

39. J. Moreland, A. Adams, and P. K. Hansma, Efficiency of light emission from surface plasmons, *Phys. Rev. B* **25** (1982) 2297, `https://doi.org/10.1103/PhysRevB.25.2297`

40. P. B. Johnson and R. W. Christy, Optical constants of transition metals: Ti, V, Cr, Mn, Fe, Co, Ni, and Pd, *Phys. Rev. B* **9** (1974) 5056, `https://doi.org/10.1103/PhysRevB.9.5056`

41. A. Vial *et al.*, Improved analytical fit of gold dispersion: Application to the modeling of extinction spectra with a finitedifference time-domain method, *Phys. Rev. B* **71** (2005) 085416, `https://doi.org/10.1103/PhysRevB.71.085416`

42. D. Barchiesi and T. Grosges, Fitting the optical constants of gold, silver, chromium, titanium, and aluminum in the visible bandwidth, *J. Nanophotonics* **8** (2014) 083097, `https://doi.org/10.1117/1.JNP.8.083097`

43. D. Barchiesi and T. Grosges, Errata: Fitting the optical constants of gold, silver, chromium, titanium and aluminum in the visible bandwidth, *J. Nanophotonics* **8** (2015) 089996, `https://doi.org/10.1117/1.JNP.8.089996`

44. A. P. Vinogradov *et al.*, Exciting surface plasmon polaritons in the Kretschmann configuration by a light beam, *Phys. Rev. B* **97** (2018) 235407, `https://doi.org/10.1103/PhysRevB.97.235407`

45. E. Ley-Koo, Recent progress in confined atoms and molecules: Superintegrability and symmetry breakings, *Rev. Mex. Fis.* **64** (2018) 326, `https://doi.org/10.31349/RevMexFis.64.326`

46. D. J. Griffiths, Introduction to electrodynamics, 2nd ed. (Prentice Hall, Englewood Cliffs, NJ, 1989), pp. 331-334.

47. S. PalDey and S. Deevi, Single layer and multilayer wear resistant coatings of (Ti,Al)N: a review, *Mat. Sci. Eng. A* **342** (2003) 58, `https://doi.org/10.1016/S0921-5093(02)00259-9`